Phase competition in a one-dimensional three-orbital Hubbard-Holstein model

Shaozhi Li,[1] Yanfei Tang,[2] Thomas A. Maier,[3,4] and Steven Johnston[1,5]
[1]*Department of Physics and Astronomy, The University of Tennessee, Knoxville, Tennessee 37996, USA*
[2]*Department of Physics, Virginia Tech, Blacksburg, Virginia 24061, USA*
[3]*Center for Nanophase Materials Sciences, Oak Ridge National Laboratory, Oak Ridge, Tennessee 37831, USA*
[4]*Computational Sciences and Engineering Division, Oak Ridge National Laboratory, Oak Ridge, Tennessee 37831, USA*
[5]*Joint Institute of Advanced Materials at The University of Tennessee, Knoxville, Tennessee 37996, USA*

(Received 14 February 2018; published 10 May 2018)

We study the interplay between the electron-phonon (*e*-ph) and on-site electron-electron (*e*-*e*) interactions in a three-orbital Hubbard-Holstein model on an extended one-dimensional lattice using determinant quantum Monte Carlo. For weak *e*-*e* and *e*-ph interactions, we observe a competition between an orbital-selective Mott phase (OSMP) and a (multicomponent) charge-density-wave (CDW) insulating phase, with an intermediate metallic phase located between them. For large *e*-*e* and *e*-ph couplings, the OSMP and CDW phases persist, while the metallic phase develops short-range orbital correlations and becomes insulating when both the *e*-*e* and *e*-ph interactions are large but comparable. Many of our conclusions are in line with those drawn from a prior dynamical mean-field theory study of the two-orbital Hubbard-Holstein model [Phys. Rev. B **95**, 121112(R) (2017)] in infinite dimension, suggesting that the competition between the *e*-ph and *e*-*e* interactions in multiorbital Hubbard-Holstein models leads to rich physics, regardless of the dimension of the system.

DOI: 10.1103/PhysRevB.97.195116

I. INTRODUCTION

Multiorbital iron-based superconductors (FeSCs) remain a significant research problem in condensed-matter physics [1–3]. While most of the FeSCs host quasi-two-dimensional FeAs or FeSe layers, a quasi-one-dimensional (1D) structure was discovered recently in $BaFe_2S_3$ [4], which has spurred interest in quasi-1D multiorbital models [5–8]. $BaFe_2S_3$ has the geometry of a two-leg ladder, and its low-temperature magnetic structure is ferromagnetic (FM) in the ladder direction and antiferromagnetic (AFM) in the leg direction [4,5]. Based on its magnetic properties, and the partially filled Fe orbitals at the Fermi level [5,9], it is natural to believe that the electron-electron (*e*-*e*) interactions play a critical role in determining the characteristics of $BaFe_2S_3$ and other FeSCs [10].

To date, theoretical studies of correlated multiorbital models have revealed many new phenomena, such as a Hund metal [11–13] and the orbital-selective Mott phase (OSMP) [14–18]. These concepts are central to our understanding of FeSCs. At the same time, however, there is some evidence that the electron-phonon (*e*-ph) interaction can also be important in these materials. For example, *e*-ph interactions have been proposed as pairing mediators in FeSe monolayers grown on oxide substrates [19–24], although the idea is under debate [25–27]. Moreover, there is experimental evidence that the low-energy electronic properties of the FeSC are modified by the *e*-ph interaction, as inferred from Raman [28] and infrared spectroscopy [29], optical conductivity measurements [30], and time-resolved photoemission [31]. On a theoretical front, early *ab initio* calculations found that the *e*-ph coupling strength in FeSCs is minimal, with total dimensionless couplings $\lambda \sim 0.2$, and insufficient to establish the observed superconducting transition temperatures T_c [32]. Several follow-up studies have examined the influence of electronic and magnetic correlations and orbital degrees of freedom on the *e*-ph interaction in multiorbital systems [27,31,33–36]. Each has found nontrivial effects and enhanced couplings, indicating that the role of the *e*-ph interaction may be more subtle than initially expected. Studying *e*-ph interactions in multiorbital materials is, therefore, an open problem. This issue is also relevant to the quasi-1D organic superconductors of the Bechgaard and Fabre salt families [37].

A simplified class of models describing the combined *e*-ph and Coulomb interactions are the Hubbard-Holstein (HH) models. In the single-band case, the competition between local Coulomb repulsion and the attractive *e*-ph interaction leads to a phase transition between antiferromagnetic and charge-density-wave (CDW) order at half-filling [38–44]. This phase transition has been studied extensively in different dimensions [38,39,42], as a function of doping [42,43,45], and using many different methods [38,39]. For example, an early dynamical mean-field theory (DMFT) study on the Bethe lattice found that this phase transition is continuous for small *e*-ph couplings and discontinuous for large couplings [39,46]. This conclusion differs from that of determinant quantum Monte Carlo (DQMC) calculations on a two-dimensional lattice, which found that the phase transition remains continuous for large couplings at high temperatures [38,47]. The phase transition in the one-dimensional HH model is also complicated. No Mott phase transition occurs in the absence of the *e*-ph interaction, and the Mott-insulating phase exists for any on-site Coulomb repulsion $U > 0$ [48]. Conversely, in the absence of *e*-*e* interactions, the critical value of the *e*-ph coupling strength exists for the formation of a CDW phase due to quantum fluctuations of the phonon field [49–52]. Retardation effects are also more prominent in one dimension at strong couplings [49,53] when

compared with the infinite-dimensional case [39]. Thus, while a variety of techniques find a robust phase transition between the CDW and the Mott phases in all dimensions, the details of the transition can differ in important ways. It is therefore important to study HH models in different dimensions and to use different approaches to obtain a complete physical picture.

Another critical factor in the single-band HH model is the degree of electron doping. For example, at half-filling, the CDW and antiferromagnetic Mott phases are separated by a metallic phase at weak e-ph coupling on the Bethe lattice [46]. But at small hole doping, phase separation of the CDW and the metallic phases [54] occurs. In two dimensions and at a quarter filling, a charge-ordered antiferromagnetic phase appears for strong Coulomb repulsion instead of the usual $\mathbf{Q} = (\pi/a, \pi/a)$ antiferromagnetic phase [55]. For quarter filling in one dimension, and at weak e-ph coupling, the antiferromagnetic phase separates into an antiferromagnetic phase and a correlated singlet phase [56]. These results indicate that many new states can arise in the doped single-band HH model. It is then natural to wonder how orbital degrees of freedom enter into this problem.

To date, multiorbital extensions of the HH model have received comparably less attention [35,57–61]. In Ref. [35], some of the current authors examined orbital-selective behaviors in a degenerate two-orbital HH model (with inequivalent bandwidths) at half-filling using single-site DMFT [35]. We found that the combined e-ph and on-site e-e interactions resulted in many competing phases including metallic, Mott, and CDW insulating phases, an OSMP, and a lattice-driven orbital-selective Peierls insulator (OSPI) analog to the OSMP.

Our prior study was carried out in infinite dimensions, where DMFT is exact; however, given the dependence on dimensionality found for the single-orbital HH model, it is essential to study the problem in other dimensions, as a function of doping, and with different techniques. Motivated by this, here we present a complementary study of the three-orbital HH model defined on an extended 1D chain at an average electron filling $\langle \hat{n} \rangle = 4$. We study the model using DQMC, which is a nonperturbative auxiliary-field technique capable of handling both the e-e and e-ph interactions on an equal footing.

Previous studies of this three-orbital 1D Hubbard model found that it exhibits a rich variety of phases including block antiferromagnetism, ferromagnetism, and several types of OSMPs [7,8,18]. As such, the model provides an excellent starting point for studying the impact of the e-ph coupling on such physics. Our results show that the e-ph interaction further modifies the boundaries of these phases by introducing additional competition with the CDW tendencies. By working on an extended lattice, we can study momentum-resolved quantities. Our main results are summarized in Fig. 1, which provides a schematic of the phase diagram of the model. (A more precise diagram with quantitative boundaries is provided at the end of our analysis; see Fig. 11.) We find four distinct regions in the λ-U parameter space, where λ and U parametrize the e-ph and e-e interactions, respectively. For small λ and large U we find an OSMP phase consistent with a block antiferromagnetic OSMP reported in prior work [7,8]. For large λ and small U we find an insulating CDW phase with mixed q ordering. These two phases are separated by a metallic (M) phase at weak λ and U, which persists into the region where U and λ are comparable to one another; however, if the two interactions are made sufficiently large but still comparable, the metallic state develops short-range orbital correlations (OCs), resulting in insulating behavior. Our results show that metallicity can be lost in the presence of large e-e and e-ph interactions due to the formation of short-range correlations. We also demonstrate that the addition of e-ph interactions to multiorbital Hubbard models can strongly influence the phases of the model and that this occurs irrespective of the dimension, filling, or mechanism underlying other orbital-selective behaviors.

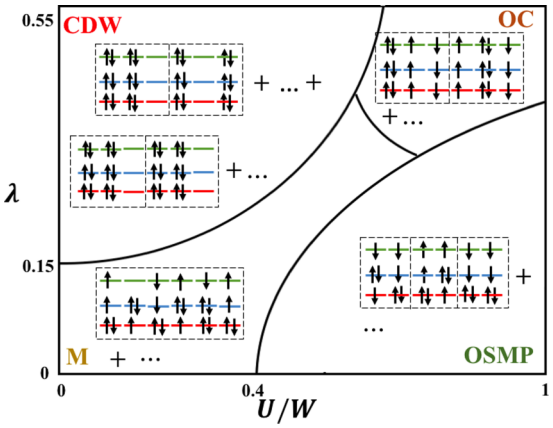

FIG. 1. A sketch of the λ-U phase diagram for our model as inferred from our DQMC calculations. Four distinct regions are found, which include states with metallic (M) characteristics, an orbital-selective Mott region (OSMP), a charge-density-wave (CDW) order, and a region with strong orbital correlations (OC) and insulating characteristics. The level diagrams sketch the dominant electronic configurations in each region. Here, W denotes the electronic bandwidth.

II. METHODS

A. Model Hamiltonian

Our starting point is a simplified one-dimensional three-orbital Hubbard model, first introduced in Ref. [7]. We then add a Holstein-type interaction, where the atomic displacement is coupled to the electron density on each orbital. The full Hamiltonian is $H = H_0 + H_{e\text{-}e} + H_{\text{lat}} + H_{e\text{-ph}}$, where

$$H_0 = -\sum_{\substack{\langle i,j\rangle \\ \sigma,\gamma,\gamma'}} t_{\gamma\gamma'} c^{\dagger}_{i,\gamma,\sigma} c_{j,\gamma',\sigma} + \sum_{i,\sigma,\gamma} (\Delta_\gamma - \mu)\hat{n}_{i,\gamma,\sigma} \quad (1)$$

are the noninteracting electronic terms,

$$H_{\text{lat}} = \sum_i \left[\frac{\hat{P}_i^2}{2M} + \frac{M\Omega^2}{2} \hat{X}_i^2 \right] = \Omega \sum_i \left(b_i^{\dagger} b_i + \frac{1}{2} \right) \quad (2)$$

are the noninteracting lattice terms,

$$H_{e\text{-}e} = U \sum_{i,\gamma} \hat{n}_{i,\gamma,\uparrow}\hat{n}_{i,\gamma,\downarrow} + \left(U' - \frac{J}{2} \right) \sum_{\substack{i,\sigma,\sigma' \\ \gamma < \gamma'}} \hat{n}_{i,\gamma,\sigma}\hat{n}_{i,\gamma',\sigma'} + J \sum_{i,\gamma<\gamma'} S^z_{i,\gamma} S^z_{i,\gamma'} \quad (3)$$

are the on-site Hubbard and Hund's interaction terms, and

$$H_{e\text{-ph}} = \alpha \sum_{i,\gamma,\sigma} \hat{X}_i \hat{n}_{i,\gamma,\sigma} = g \sum_{i,\gamma,\sigma} (b_i^\dagger + b_i)\hat{n}_{i,\gamma,\sigma} \tag{4}$$

are the e-ph coupling terms. Here, $\langle \cdots \rangle$ denotes a sum over nearest neighbors; $c^\dagger_{i,\gamma,\sigma}$ ($c_{i,\gamma,\sigma}$) creates (annihilates) a spin σ electron in orbital $\gamma = 1,2,3$ on site i; $b_i^\dagger$ (b_i) creates (annihilates) a phonon on lattice site i; $S^z_{i,\gamma}$ is the z component of the spin operator $\mathbf{S}_{i,\gamma}$; $\hat{n}_{i,\gamma,\sigma} = c^\dagger_{i,\gamma,\sigma} c_{i,\gamma,\sigma}$ is the number operator; and $\hat{X}_i$ and $\hat{P}_i$ are the lattice position and momentum operators, respectively. The parameters Δ_γ are the on-site energies for each orbital, $t_{\gamma,\gamma'}$ are the intra- and interorbital hopping integrals, U and U' are the intra- and interorbital Hubbard interactions, respectively, and J is Hund's coupling. The parameter $g = \frac{\alpha}{\sqrt{2M\Omega}}$ is the strength of the e-ph coupling and Ω is the phonon energy. Finally, μ is the chemical potential, which fixes the average particle number.

In Eq. (3) we have neglected the pair-hopping and spin-flip terms of Hund's interaction, as was done in Ref. [18] for the same model without e-ph interactions. These terms introduce a significant fermion sign problem [62] for our DQMC calculations and are therefore neglected to make the problem tractable. Prior work [8] has shown that these terms only change the location of the various phase boundaries for the model considered here in the absence of the e-ph interaction. We proceed, therefore, assuming that this will also hold true once the phonons are included in our calculations.

B. Model parameters

Throughout this work, we choose $U' = U - 2J$, as is standard for enforcing rotational symmetry [63], although we have neglected the pair-hopping and spin-flip terms in Eq. (3). We further vary U while holding $J = U/4$ fixed. This choice produces a robust OSMP [7,8,18] in the absence of the e-ph interaction and is appropriate for the FeSCs. We work at a fixed filling $\langle \hat{n} \rangle = 4$, which is typical for three-orbital Hubbard models used to describe the 2D FeSCs [64]. We expect that the same filling is needed to describe the quasi-one-dimensional system $BaFe_2S_3$. This choice of filling also allows us to make direct comparisons to previous studies in the absence of the e-ph interaction [7,8,18]. In this spirit, we also set $t_{11} = t_{22} = -0.5$ eV, $t_{33} = -0.15$ eV, $t_{13} = t_{23} = 0.1$ eV, $t_{12} = 0$ eV, $\Delta_1 = -0.1$ eV, $\Delta_2 = 0$ eV, $\Delta_3 = 0.8$ eV, and $\Omega = 0.5$ eV, again following Refs. [18] and [7]. The total bandwidth of the noninteracting model is $W = 2.45$ eV, which serves as the unit energy. The dimensionless e-ph coupling constant is defined as $\lambda = \alpha^2/(M\Omega^2 W)$. (Note that since this is a multiband system, different choices of bandwidths are possible. Here, we select the total bandwidth, as was done in Ref. [35].) Finally, we set $a = M = 1$ as units of distance and mass, respectively, and work at an inverse temperature $\beta = 14.7/W$ unless stated otherwise; this temperature is low enough to identify the ordering tendencies in the model.

C. Methods

We use DQMC to solve the 1D three-orbital HH model. The general details of the method can be found in Refs. [65–67], while the aspects that are unique to the Holstein phonons can be found in Refs. [47] and [68]. Throughout this work, we use a one-dimensional chain with a chain size $N = 16$ and imaginary-time discretization of $\Delta\tau = 0.245/W$, unless otherwise stated. In all of our simulations, we have not observed significant $\Delta\tau$ errors introduced by this choice.

DQMC calculates the electron Green's function $G(k,\tau)$ defined in the imaginary-time τ axis. In Sec. III B we will examine the spectral properties of our model, which requires an analytic continuation to the real frequency axis. Here, we used the maximum-entropy method (MEM) [69,70].

III. RESULTS

In this study, we will focus on the four phases resulting from the competition between on-site Coulomb repulsion and the e-ph interaction. The four phases are metal, charge-density-wave phase, orbital-selective Mott phase, and orbital-correlated state, as shown in Fig. 1. They are identified by examining the evolution of the single and double occupations on each orbital, the spectral weight, and the charge-density-wave susceptibility. We will discuss the particular variation of these quantities as a function of parameters in the following sections.

A. Weak electron-phonon coupling

Previous studies of this model without phonons showed that an OSMP forms for U values in the range $0.6 < U/W < 2$ for our choice of J. In this state, orbital 3 becomes insulating while the remaining orbitals host itinerant electrons [7,8]. The onset of this phase is signaled by the fact that the filling on orbital 3 is $\langle \hat{n}_3 \rangle = 1$. For $U/W > 2$, orbitals 1 and 2 retain a noninteger filling but are driven into an insulating state by the onset of short-range orbital ordering [18]. To avoid this complication, we restrict ourselves to the $U/W < 1$ region.

We now examine the impact of the e-ph interaction on the OSMP. Figure 2 plots the electronic occupations of the three orbitals for different values of U/W and λ. For $\lambda = 0$, Fig. 2(c) shows that $\langle \hat{n}_3 \rangle$ converges to 1 as U/W increases, implying that a Mott gap is formed on this orbital for $U/W \geqslant 0.4$. At the same time, $\langle \hat{n}_1 \rangle$ and $\langle \hat{n}_2 \rangle$ maintain noninteger values, implying that these orbitals remain itinerant [see Figs. 2(a) and 2(b)]. These results are consistent with previous studies [7,8]. When we include the e-ph coupling, the orbital occupations are modified significantly. For example, Figs. 2(d)–2(f) show that the e-ph coupling tends to make electronic occupations on all three orbitals uniform when $U/W < 0.4$, with the average filling on each orbital approaching $\langle \hat{n}_\gamma \rangle = \frac{4}{3}$ when λ is large. This value of the occupation on each orbital is consistent with a charge-ordered state where two sites are fully occupied and one site is empty, which is shown in the CDW region of Fig. 1. This kind of charge order arises from the attractive interaction mediated by the e-ph interaction [71]. For the fully occupied site, the attractive interaction can be mapped into a negative effective U for all three orbitals at this site in the large-Ω limit. For an empty site, the effective interaction is not modified by the e-ph coupling. Therefore, the effective Hubbard interaction is not uniform in real space if there is a density modulation. When the e-ph coupling is strong, this nonuniform attractive interaction can produce a charge-ordered state but with a

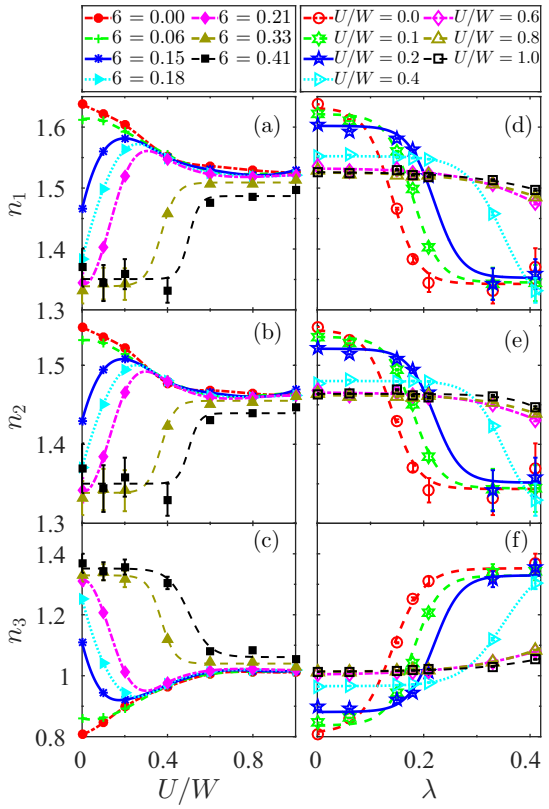

FIG. 2. The variation of electronic densities on the three orbitals as a function of the Hubbard U and the e-ph coupling strength λ. Panels (a)–(c) show the variation of electronic densities as a function of the Hubbard U on orbitals $\gamma = 1, 2$, and 3, respectively. Similarly, panels (d)–(f) show the change of electronic densities as a function of λ on the same three orbitals. In each panel, error bars smaller than the marker size have been suppressed for clarity, and a smoothing spline is used as a guide to the eye.

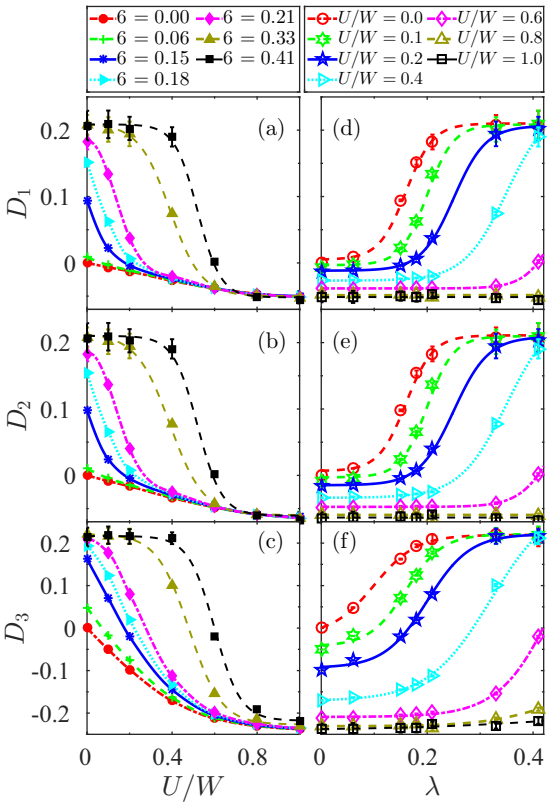

FIG. 3. The variation of double occupancies on the three orbitals as a function of the Hubbard U and the e-ph coupling strength λ. Panels (a)–(c) show the variation of double occupancies as a function of the Hubbard U on orbitals $\gamma = 1, 2$, and 3, respectively. Similarly, panels (d)–(f) show the change of double occupancies as a function of λ on the same three orbitals. In each panel, error bars smaller than the marker size have been suppressed for clarity, and a smoothing spline is used as a guide to the eye.

uniform average occupation on each orbital. The transition from a CDW phase to an OSMP can be seen in Fig. 2(c), where $\langle \hat{n}_3 \rangle$ decreases from $\frac{4}{3}$ to 1 at $\lambda = 0.33$. Increasing the e-ph coupling pushes this transition to larger values of U/W; for example, for $\lambda = 0.41$ it occurs at $U/W \sim 0.5$.

The competition between the CDW and OSMP tendencies is also manifest in the behavior of the orbital's double occupation $D_\gamma = \langle \hat{n}_{\gamma,\uparrow} \hat{n}_{\gamma,\downarrow} \rangle - \langle \hat{n}_{\gamma,\uparrow} \rangle \langle \hat{n}_{\gamma,\downarrow} \rangle$, as summarized in Fig. 3. When the phonon-mediated effective attraction overcomes the Coulomb repulsion, we expect $D_\gamma > 0$; otherwise, $D_\gamma < 0$. Figures 3(a)–3(c) present D_γ as a function of U/W for fixed values of λ, where we find that D_γ decreases as U is increased, and D_3 converges to $-\frac{1}{4}$ in the limit of a strong Hubbard interaction, consistent with a Mott-insulating state where double occupation is suppressed. Figures 3(d)–3(f) alternatively plot the data as a function of λ for fixed values of U/W. Here, we find that for $U/W < 0.4$, D_γ increases as λ increases and converges to $\frac{2}{9}$ on each orbital. This value is consistent with the double occupations expected for the CDW phase shown in Fig. 1.

The electronic density and double occupations provide indirect evidence of the CDW phase. To obtain more direct evidence of a CDW order, we calculated the charge susceptibility

$$\chi^c_{\gamma,\gamma'}(q) = \frac{1}{N} \int_0^\beta d\tau \langle \hat{n}_{q,\gamma}(\tau) \hat{n}_{q,\gamma'}(0) \rangle, \tag{5}$$

where q is the momentum, τ is the imaginary time, $\hat{n}_{q,\gamma} = \sum_{i,\sigma} e^{iqR_i} \hat{n}_{i,\gamma,\sigma}$, and R_i is a lattice vector.

Figure 4 shows the momentum dependence of the three intraorbital charge susceptibilities for $U/W = 0$ and different e-ph coupling strengths. At weak coupling (i.e., $\lambda = 0.0$ and 0.06), $\chi^c_{\gamma,\gamma}(q)$ is small, with no clear peak at any momenta. This observation implies that a finite value of λ is needed for charge correlations to develop at this temperature, and is consistent with the one-dimensional Holstein model [43]. As the value of λ is increased, a clear peak structure forms in $\chi^c_{\gamma\gamma}(q)$. For instance, already at $\lambda = 0.18$ we find a peak centered at $q = \pi/a$ for all three orbitals, indicating the formation of a two-sublattice charge correlation at $\beta = 14.7/W$. Upon further cooling of the system, we find that additional charge correlations develop at a second q point. For example, Fig. 5 compares $\chi^c_{\gamma,\gamma}(q)$ at $\beta = 14.7/W$ and $49/W$ for the $\lambda = 0.15$ and $U/W = 0$ case. For temperature $\beta = 14.7/W$, $\chi^c_{\gamma,\gamma}(q)$ has a single peak at $q = \pi/a$; however, as the temperature is decreased to $\beta = 49/W$, $\chi^c_{\gamma,\gamma}(q)$ increases and a second peak

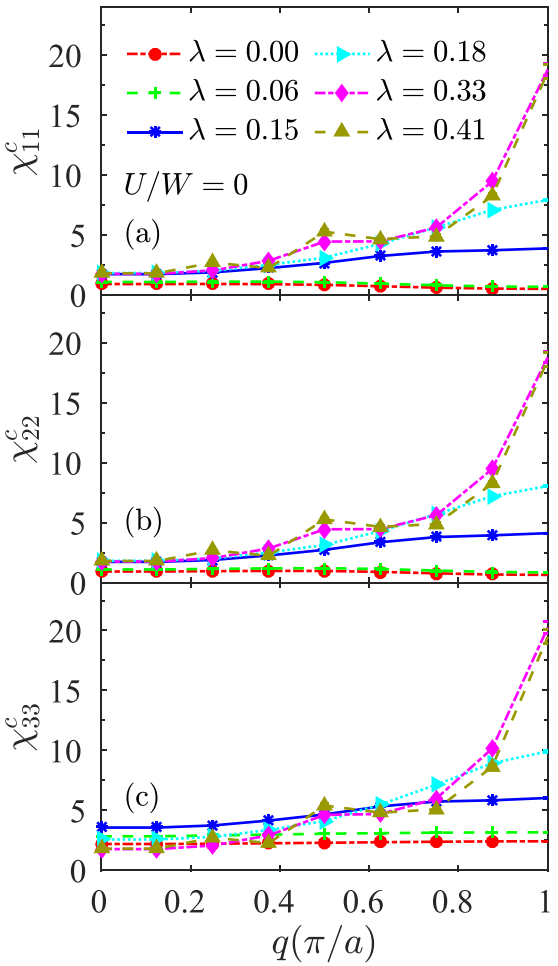

FIG. 4. Momentum dependence of charge correlation function $\chi^c_{\gamma,\gamma}(q)$ for orbital 1 (a), orbital 2 (b), and orbital 3 (c) at different λ values. The Hubbard $U/W = 0$. In each panel, error bars smaller than the marker size have been suppressed for clarity.

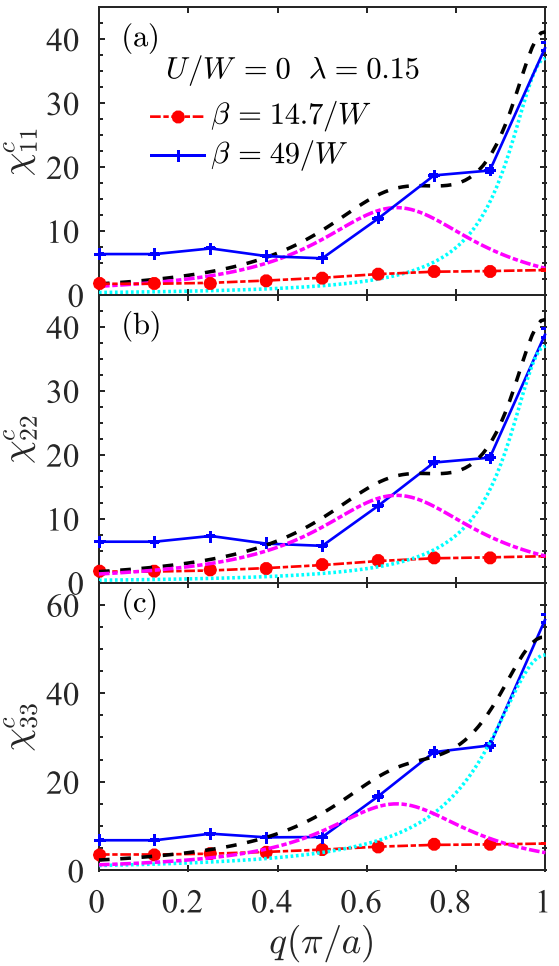

FIG. 5. Momentum dependence of charge correlation function $\chi^c_{\gamma,\gamma}(q)$ for orbital 1 (a), orbital 2 (b), and orbital 3 (c) at different β values. The Hubbard $U/W = 0$ and $\lambda = 0.15$. The black dashed lines are eye-guided lines for a combination of two Lorentzian functions with different peak positions. The two Lorentzian functions are shown with dotted and dash-dotted lines, respectively. In each panel, error bars smaller than the marker size have been suppressed for clarity.

forms at $q \sim 2\pi/3 - 3\pi/4$, which is evident as a shoulder in $\chi^c_{\gamma,\gamma}(q)$. To better recognize these two peaks, we plot as a guide-to-the-eye the sum of two Lorentzian functions centered at $q = 2\pi/3a$ (dash-dotted line) and $q = \pi/a$ (dotted line).

The two peak structures in $\chi^c_{\gamma,\gamma}(q)$ likely reflect different ordering tendencies. The charge configurations sketched in Fig. 1 are consistent with $q_1 \approx 2\pi/3a$ and $q_2 = \pi/a$ orderings. We propose, therefore, that the CDW state is characterized by a superposition of $|\ldots 660660\ldots\rangle$ and $|\ldots 606660\ldots\rangle$ configurations along the chain, where the number indicates the number of carriers on each site. These charge configurations are consistent with the values of the orbitally resolved single and double occupancies discussed previously. In fact, these two peaks reflect two different values of $2k_F$ that appear in this multiorbital model; the Fermi momentum for orbitals 1 and 2 is $\sim 0.33\pi/a$, while the Fermi momentum for orbital 3 is $\sim 0.5\pi/a$. Thus, these two peak values correspond to $q = 2k_F$ in the weak-coupling limit, where the CDW tendencies are driven primarily by nesting conditions. When we increase the e-ph coupling further, the k_F for orbitals 1 and 2 increases to $0.5\pi/a$. Therefore, we expect that only one peak will be observed in the charge-density-wave susceptibility in the limit of strong e-ph coupling.

We now turn to the spectral weight of the three orbitals in the vicinity of the Fermi level E_F to assess whether the various phases we observe are insulating or not. The spectral weight can be estimated directly from the imaginary-time Green's function using the relationship [72]

$$\beta G_\gamma(r = 0, \beta/2) = \beta \sum_k \int d\omega \, \mathrm{sech}(\beta\omega/2) A_\gamma(k,\omega), \quad (6)$$

where $A_\gamma(k,\omega)$ is the orbitally resolved spectral function. At low temperature, the function $\beta\,\mathrm{sech}(\beta\omega/2)$ is sharply peaked around $\omega = E_F = 0$ and thus provides a measure of the spectral weight integrated over a window of a few β^{-1} of E_F.

Figure 6 plots $\beta G_\gamma(r = 0, \beta/2)$ for the three orbitals for different values of U/W and λ. In Figs. 6(a)–6(c), the spectral weight of each orbital is plotted as a function of U for fixed λ. In the absence of the e-ph interaction ($\lambda = 0$), the spectral weight of all three orbitals decreases as the Hubbard

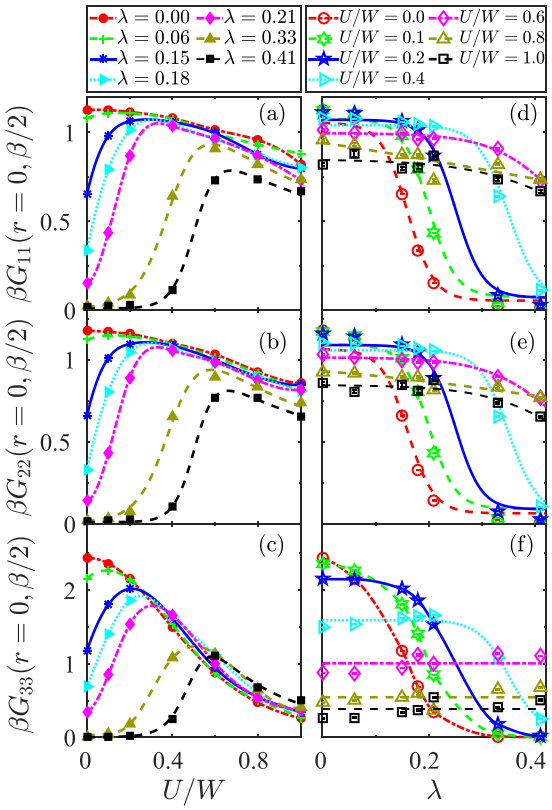

FIG. 6. The variation of the spectral weight for the three orbitals as a function of the Hubbard U and the e-ph coupling strength λ. Panels (a)–(c) show the variation of spectral weights as a function of the Hubbard U for three orbitals, respectively. Panels (d)–(f) show the change of spectral weights as a function of λ for three orbitals, respectively. In each panel, error bars smaller than the marker size have been suppressed for clarity, and a smoothing spline is used as a guideline to the eye.

U increases. However, the spectral weight on orbital $\gamma = 3$ decreases more rapidly than the other two orbitals, consistent with the formation of an OSMP [18]. [The small but nonzero value of $\beta G_3(r = 0, \beta/2)$ is due to the elevated temperature of the simulation.] As the value of λ increases, we begin to see the loss of spectral weight in all three orbitals when U/W is small.

Figures 6(d)–6(f) plot $\beta G_\gamma(r = 0, \beta/2)$ as a function of λ for fixed U/W. For $U/W = 0$, the spectral weight of all three orbitals is suppressed as the e-ph coupling is increased. We further observe a sudden decrease in the spectral weight of all three orbitals for $\lambda \geqslant 0.15$, where a prominent peak in $\chi^c_{\gamma,\gamma}(k)$ is observed. Thus, for $\lambda \geqslant 0.15$ and $U/W = 0$, the system is an insulating state driven by CDW correlations. The behavior of the spectral weight is qualitatively similar for $U/W < 0.2$, however the transition to the CDW phase occurs at larger values of λ as U/W increases. Based on these results, we conclude that the CDW phase is insulating.

Unlike the OSMP, we do not find any orbital-selective behavior associated with the formation of the CDW phase; the rate at which the spectral weight approaches zero appears to be the same for all three orbitals at this temperature. This result is in contrast to the degenerate two-orbital case with inequivalent bandwidths [35], where orbital-selective CDW behavior was found. This difference could be attributed to changes in the total bandwidth, dimensionality, or model. (For example, the current model has inequivalent bandwidths and crystal-field splittings, while the former only had inequivalent bandwidths.) Further studies will be needed to better understand the differences between these two cases.

We now return to the competition between the OSMP and CDW phases. Figures 6(a)–6(c) reveal that the spectral weight decreases as the strength of the e-ph is increased when U/W is small. For a fixed value of $\lambda \neq 0$, $\beta G_\gamma(r = 0, \beta/2)$ initially increases with U/W before reaching a maximum value and decreases along the U axis. This behavior reflects the competition between the e-ph and the e-e interactions [38,73]. At small U/W the CDW correlations dominate, for large U/W the OSMP correlations dominate, and for intermediate values of λ a metallic phase is realized.

B. Spectral properties of the CDW phase

The spectral function of the OSMP was studied in detail in Ref. [18] in the absence of e-ph interactions. We will focus, therefore, on the spectral function of the CDW phase. Figure 7 shows the spectral function for $U = 0$ and $\lambda = 0.33$ and its orbitally resolved components. The system is insulating, with a large CDW gap and broadened spectral features, consistent with our spectral weight analysis. The upper bands of three orbitals have dispersions with a clear folded shape, while the lower bands of orbitals 1 and 2 have a more cosinelike dispersion. This cosinelike shape arises from the combination of an incoherent peak and an additional peak arising from thermally activated transitions to states with additional phonons excited [74]. To better recognize these two peaks, Figs. 7(e)–7(l) plot the spectral functions at fixed momentum $k = 0$, π/a, $\pi/4a$, and $3\pi/4a$ for orbitals 1 and 2. The red dashed curve denotes Lorentzian fits of the data allowing for an incoherent peak above and below the Fermi level and an additional thermally excited peak below the Fermi level. The fitting results are consistent with the Maxent results. We find that the thermally excited state is located around $E = -2.5$ eV and is momentum-independent, consistent with previous results for the one-dimensional single-band spinless Holstein model [74]. The folded band is observed at $k = 0$ and $k = \pi/a$ and at $k = \pi/4a$ and $k = 3\pi/4a$, respectively. The intensity of the incoherent peak below the Fermi level in the folded band is much weaker than that of the thermally excited peak, leading to a cosine shape observed in the upper panels of Fig. 7.

C. Strong electron-phonon coupling

Our previous single-site DMFT study of the two-orbital HH model at half-filling observed a direct transition between the OSMP and CDW phase in the strong e-ph coupling limit [35], with no intervening metallic phase. In contrast, for the current model, we find evidence for an orbitally correlated insulating state located between the CDW phase and OSMP at strong couplings. Figure 8 shows the spectral function [Fig. 8(a)] and its three orbitally resolved components [Figs. 8(b)–8(d)] at $U/W = 1$, $\lambda = 0.6$, and $\beta = 29.4/W$, where a gap is

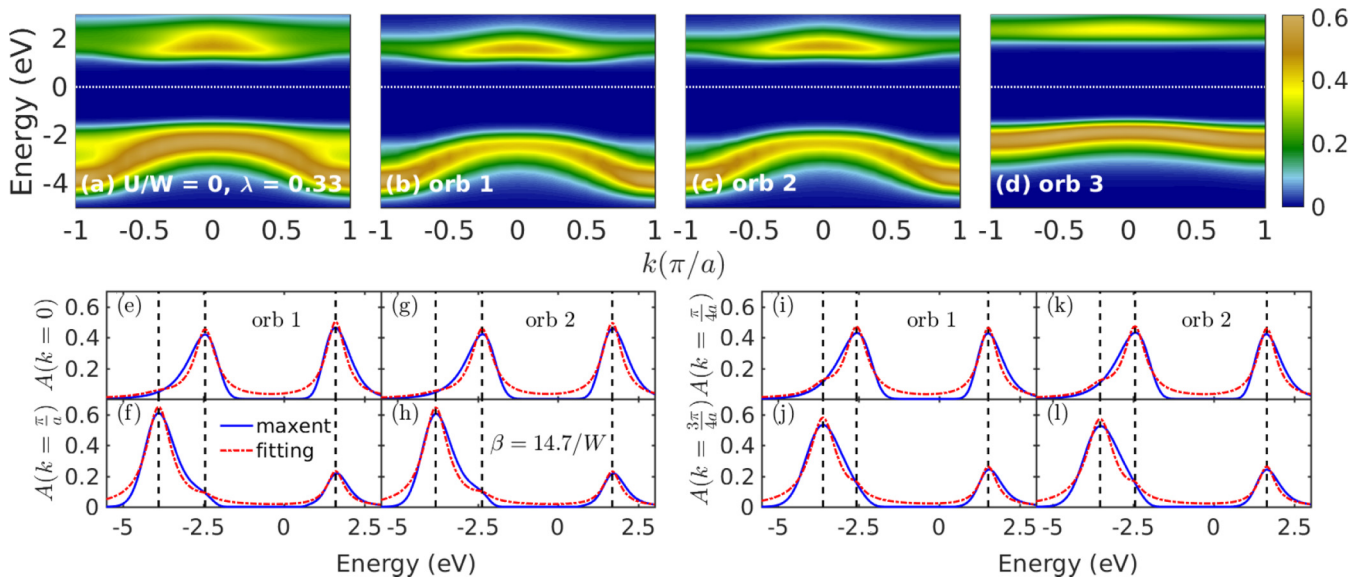

FIG. 7. Spectral functions for $U = 0$ and $\lambda = 0.33$. Panels (b), (c), and (d) are the orbital 1, 2, and 3 components of the spectral function in (a), respectively. Panels (e), (f), (i), and (j) are spectral functions of the orbital 1 at momentum $k = 0$, $k = \frac{\pi}{a}$, $k = \frac{\pi}{4a}$, and $\frac{3\pi}{4a}$, respectively. Similarly, (g), (h), (k), and (l) are spectral functions of the orbital 2 at those four momenta. The black dashed lines show three peak positions in the maximum entropy results. The red dotted lines are Lorentzian fitting results.

clearly observed. The spectral function is similar to the CDW case shown in Fig. 8, however the origin of the gap is not CDW correlations since $\chi^c_{\gamma,\gamma'}(q)$ (not shown) is small in this state. Also, the double occupation $D_\gamma \approx -\frac{1}{9} < 0$ (see Fig. 2), indicating the Coulomb interaction is the dominant interaction in this phase.

The nature of this OC phase is sketched on the left side of Fig. 9. It consists of one site where all three orbitals are fully occupied and two neighboring sites that are half-filled and in a high-spin state. This electronic configuration is consistent with the observed orbital occupations and the value of the double occupation $D_\gamma = -\frac{1}{9}$.

In the HH model, the intra- and interorbital Hubbard interactions U_{eff} and U'_{eff} are renormalized by the e-ph interaction, and the ground state can change based on the value of these effective Hubbard interactions. Figures 9(a) and 9(b) show two types of charge fluctuations that are possible within the proposed OC state. The potential energy costs of these fluctuations are PE $\sim U_{\text{eff}} + J$ and PE $\sim -2(U'_{\text{eff}} - J)$, respectively. To estimate the magnitude of these energies, we performed an exact diagonalization calculation in the atomic limit and compared the ground-state energies of the shown atomic configurations. For $U/W = 1$ and $\lambda = 0.6$, we find that these two potential energies are 1.305 and 0.815 eV, respectively. When the orbital hybridization is introduced, the total potential energy cost is compensated for by a kinetic energy gain of KE $\approx t_{11} = 0.5$ eV. However, the ratio $\frac{\text{PE}}{\text{KE}} > 1$ in both cases, suggesting that charge fluctuations are suppressed, and the system will be insulating. The conditions for forming the OC insulating state are then $U'_{\text{eff}} - J < 0$ and $U_{\text{eff}} + J > 0$, which in turn requires that the e-ph coupling strength is not too strong; otherwise, the CDW phase is formed. (Note that a larger Hund's coupling favors satisfying these two conditions.) In the OC insulating state, the fully occupied site and two half-occupied sites can be arranged randomly in a long chain as the energy cost will not change. Therefore, short-range orbital correlations would be sufficient to produce insulating behavior at finite temperature.

We can confirm the presence of OC by examining the equal-time orbital correlation function

$$T_{\gamma\gamma'}(d) = \frac{1}{N}\sum_i \langle(\hat{n}_{i+d,\gamma} - \hat{n}_{i+d,\gamma'})(\hat{n}_{i,\gamma} - \hat{n}_{i,\gamma'})\rangle. \quad (7)$$

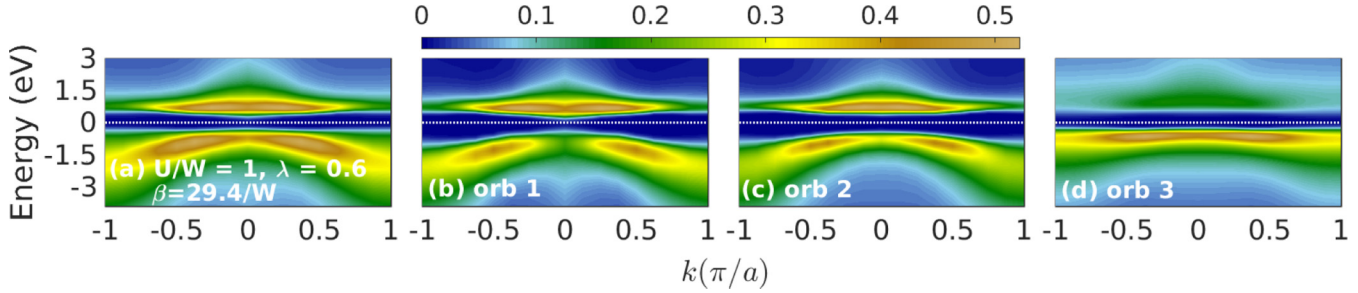

FIG. 8. Spectral functions for $U/W = 1$ and $\lambda = 0.6$. Panels (b), (c), and (d) are the orbitals 1, 2, and 3 components of the spectral function in (a). The inverse temperature is $\beta = 29.4/W$. The white dotted line is the Fermi surface.

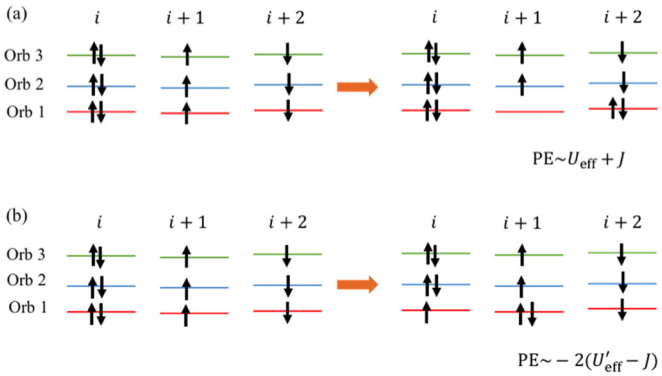

FIG. 9. Cartoon sketch of the relevant charge-fluctuation processes leading to the orbital ordered insulating state when $U/W = 1$ and $\lambda = 0.6$.

The charge configuration expected for the OC shown in Fig. 9 would produce an orbital correlation function $T_{\gamma\gamma'}(d) = 0$. Figure 10(b) shows the variation of the on-site orbital correlations $T_{\gamma,\gamma'}(0)$ in the phase transition from the OSMP to the OC state. In general, the correlation function for $d = 0$ is larger than that for $d \neq 0$. Thus, the on-site correlation is a good indicator for when $T_{\gamma,\gamma'}(d) \to 0$ and can be used to trace the formation of the orbital correlations. In the OSMP region, $T_{\gamma,\gamma'}(0)$ is greater than 0.1. For example, at $\lambda = 0$, $T_{1,2}(0)$, $T_{1,3}(0)$, and $T_{2,3}(0)$ are 0.16, 0.14, and 0.125, respectively. $T_{\gamma,\gamma'}(0)$ decreases slowly initially as the e-ph coupling strength is enhanced. Conversely, near the phase transition, $T_{\gamma,\gamma'}(0)$ decreases very quickly; at $\lambda = 0.6$, $T_{1,2}(0)$, $T_{1,3}(0)$, and $T_{2,3}(0)$ are 0.056, 0.061, and 0.057, respectively. The nonzero value at $\lambda = 0.6$ is likely due to the elevated temperature. We find that $T_{1,2}(0)$, $T_{1,3}(0)$, and $T_{2,3}(0)$ are decreased to 0.038, 0.03, and 0.029, respectively, as the inverse temperature is decreased to

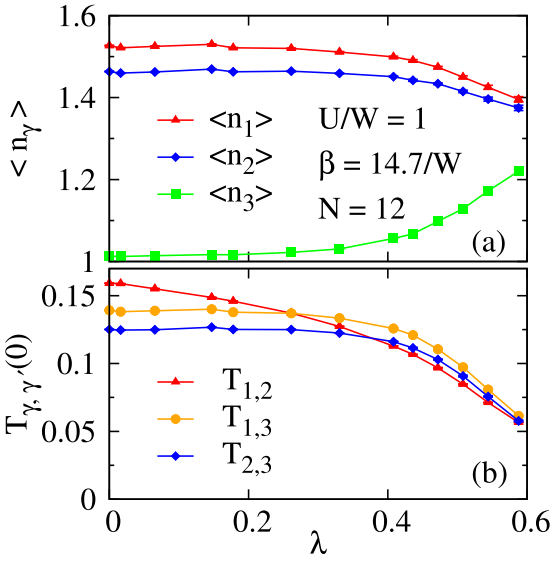

FIG. 10. (a) The electronic occupations $\langle \hat{n}_\gamma \rangle$ of orbital γ as a function of the e-ph coupling strength λ. (b) The on-site orbital correlations $T_{\gamma\gamma'}$ between orbital γ and γ' as a function of λ. These results were obtained on an $N = 12$ site chain. In each panel, error bars smaller than the marker size have been suppressed for clarity.

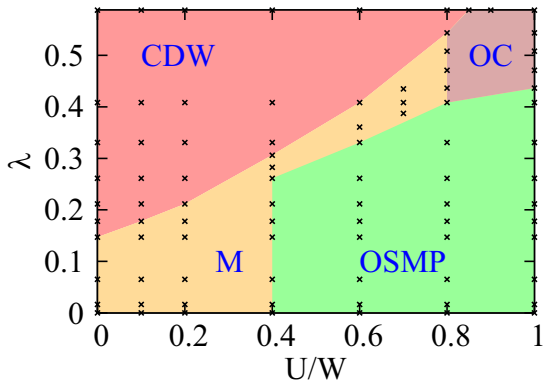

FIG. 11. The phase diagram of the three-orbital Hubbard-Holstein model for $\beta = 14.7/W$ and $\langle \hat{n} \rangle = 4$. The different phases are labeled as follows: metal (M), charge-density-wave order (CDW), orbital selective Mott phase (OSMP), and orbital correlation (OC).

$29.4/W$. We expect that the correlation function tends toward zero as $T \to 0$, and a sharp phase transition from the OSMP to the OC state would occur.

We traced the phase transition from the OSMP to the OC in Fig. 10(a), which shows the variation of orbital occupations in the phase transition from the OSMP to the OC phase at $U/W = 1$ and $\beta = 14.7/W$. Here, the chain size is $N = 12$. The critical e-ph coupling value λ_c of the phase transition from the Mott phase to the OC state is about 0.43, where $\langle \hat{n}_3 \rangle > 1$. As $U/W = 1$ and $\lambda = 0.6$, orbital occupations for three orbitals are 1.4, 1.38, and 1.22 at $\beta = 14.7/W$, respectively. Those occupations are changed to 1.346, 1.344, 1.31 at $\beta = 29.4/W$, implying that the OC state supports the same occupation on each orbital, consistent with the electron configuration shown in Fig. 9.

IV. DISCUSSION AND SUMMARY

We have performed a study of a three-orbital Hubbard-Holstein model on an extended one-dimensional chain using nonperturbative DQMC. The phase diagram of the one-dimensional model for $\beta = 14.7/W$ and $\langle \hat{n} \rangle = 4$, shown in Fig. 11, shares many similarities to the one found for an infinite-dimensional degenerate two-orbital HH model with inequivalent bandwidths [35], containing a metallic phase, a CDW phase, and an OSMP. The metallic phase is most prominent in small values of U and λ but penetrates into the region of intermediate interaction strengths separating the CDW and OSMP when $U/W \sim 2\lambda$. The critical e-ph coupling needed for the CDW phase transition at $U = 0$ in our model is $\lambda_c \sim 0.15$. The nonzero value of λ_c is consistent with results for the single-band Holstein model [43,49].

At strong couplings, we found evidence for an orbital correlation state in the phase diagram, which was not found in the previous DMFT study. We argue that this difference stems from the filling used in our model ($\langle \hat{n} \rangle = 4$ here versus $\langle \hat{n} \rangle = 2$ in Ref. [35]) and the use of an extended cluster here [18]. The OC state resides between the CDW phase and OSMP and tends to extend to large Hubbard U. This region of the phase diagram is the same one where the OSMP disappears,

and an anti-ferro-orbital correlation was found in the $\lambda = 0$ case [18]. We expect that a phase transition occurs between the anti-ferro-orbital order and the OC state at $U/W = 2$. These results show that the phase diagram of multiorbital HH models can exhibit remarkably rich physics as a function of interaction strengths, doping, and other parameters.

In the past, the *e*-ph interaction has been neglected when studying the FeSCs. As mentioned in the Introduction, this is largely motivated by early *ab initio* calculation showing that the dimensionless interaction strength λ is only about 0.2 [32]. However, we find that the electronic degrees of freedom in our 1D multiorbital model can be influenced significantly by small *e*-ph couplings. Given that a similar result was obtained in the case of a two-orbital Hubbard model in infinite dimensions using DMFT [35], these results imply that the *e*-ph interaction cannot be neglected *a priori* in multiorbital systems, and that this conclusion holds independent of the dimension of the system. We hope that this study will motivate further work in this interesting area.

ACKNOWLEDGMENTS

This work was supported by the Scientific Discovery through Advanced Computing (SciDAC) program funded by the U.S. Department of Energy, Office of Science, Advanced Scientific Computing Research and Basic Energy Sciences, Division of Materials Sciences and Engineering. CPU time was provided by resources supported by the University of Tennessee and Oak Ridge National Laboratory Joint Institute for Computational Sciences (http://www.jics.utk.edu).

[1] D. C. Johnston, The puzzle of high-temperature superconductivity in layered iron pnictides and chalcogenides, Adv. Phys. **59**, 803 (2010).

[2] G. R. Stewart, Superconductivity in iron compounds, Rev. Mod. Phys. **83**, 1589 (2011).

[3] P. C. Dai, J. P. Hu, and E. Dagotto, Magnetism and its microscopic origin in iron-based high-temperature superconductors, Nat. Phys. **8**, 709 (2012).

[4] H. Takahashi, A. Sugimoto, Y. Nambu, T. Yamauchi, Y. Hirata, T. Kawakami, M. Avdeev, K. Matsubayashi, F. Du, C. Kawashima, H. Soeda, S. Nakano, Y. Uwatoko, Y. Ueda, T. J. Sato, and K. Ohgushi, Pressure-induced superconductivity in the iron-based ladder material $BaFe_2S_3$, Nat. Mater. **14**, 1008 (2015).

[5] N. D. Patel, A. Nocera, G. Alvarez, R. Arita, A. Moreo, and E. Dagotto, Magnetic properties and pairing tendencies of the iron-based superconducting ladder $BaFe_2S_3$: Combined *ab initio* and density matrix renormalization group study, Phys. Rev. B **94**, 075119 (2016).

[6] N. Kaushal, J. Herbrych, A. Nocera, G. Alvarez, A. Moreo, F. A. Reboredo, and E. Dagotto, Density matrix renormalization group study of a three-orbital Hubbard model with spin-orbit coupling in one dimension, Phys. Rev. B **96**, 155111 (2017).

[7] J. Rincon, A. Moreo, G. Alvarez, and E. Dagotto, Exotic Magnetic Order in the Orbital-Selective Mott Regime of Multiorbital Systems, Phys. Rev. Lett. **112**, 106405 (2014).

[8] G. Liu, N. Kaushal, S. Li, C. B. Bishop, Y. Wang, S. Johnston, G. Alvarez, A. Moreo, and E. Dagotto, Orbital-selective Mott phases of a one-dimensional three-orbital Hubbard model studied using computational techniques, Phys. Rev. E **93**, 063313 (2016).

[9] Y. Zhang, L. Lin, J.-J. Zhang, E. Dagotto, and S. Dong, Pressure-driven phase transition from antiferromagnetic semiconductor to nonmagnetic metal in the two-leg ladders AFe_2X_3 ($A = $ Ba,K; $X = $ S,Se), Phys. Rev. B **95**, 115154 (2017).

[10] E. Dagotto, Colloquium: The unexpected properties of alkali metal iron selenide superconductors, Rev. Mod. Phys. **85**, 849 (2013).

[11] K. Haule and G. Kotliar, Coherence-incoherence crossover in the normal state of iron oxypnictides and importance of Hund's rule coupling, New J. Phys. **11**, 025021 (2009).

[12] A. Georges, L. de'Medici, and J. Mravlje, Strong correlations from Hund's coupling, Annu. Rev. Condens. Matter Phys. **4**, 137 (2013).

[13] L. Fanfarillo and E. Bascones, Electronic correlations in Hund metals, Phys. Rev. B **92**, 075136 (2015).

[14] V. I. Anisimov, I. A. Nekrasov, D. E. Kondakov, T. M. Rice, and M. Sigrist, Orbital-selective Mott insulator transition in $Ca_{2-x}Sr_xRuO_4$, Eur. Phys. J. B **25**, 191 (2002).

[15] A. Koga, N. Kawakami, T. M. Rice, and M. Sigrist, Orbital-Selective Mott Transitions in the Degenerate Hubbard Model, Phys. Rev. Lett. **92**, 216402 (2004).

[16] L. de'Medici, G. Giovannetti, and M. Capone, Selective Mott Physics as a Key to Iron Superconductors, Phys. Rev. Lett. **112**, 177001 (2014).

[17] M. Yi, D. H. Lu, R. Yu, S. C. Riggs, J.-H. Chu, B. Lv, Z. K. Liu, M. Lu, Y.-T. Cui, M. Hashimoto, S.-K. Mo, Z. Hussain, C. W. Chu, I. R. Fisher, Q. Si, and Z.-X. Shen, Observation of Temperature-Induced Crossover to an Orbital-Selective Mott Phase in $A_xFe_{2-y}Se_2$ (A=K, Rb) Superconductors, Phys. Rev. Lett. **110**, 067003 (2013).

[18] S. Li, N. Kaushal, Y. Wang, Y. Tang, G. Alvarez, A. Nocera, T. A. Maier, E. Dagotto, and S. Johnston, Nonlocal correlations in the orbital-selective Mott phase of a one-dimensional multiorbital Hubbard model, Phys. Rev. B **94**, 235126 (2016).

[19] D. Liu, W. Zhang, D. Mou, J. He, Y.-B. Ou, Q.-Y. Wang, Z. Li, L. Wang, L. Zhao, S. He, Y. Peng, X. Liu, C. Chen, L. Yu, G. Liu, X. Dong, J. Zhang, C. Chen, Z. Xu, J. Hu, X. Chen, X. Ma, Q. Xue, and X. J. Zhou, Electronic origin of high-temperature superconductivity in single-layer FeSe superconductor, Nat. Commun. **3**, 1946 (2012).

[20] J. J. Lee, F. T. Schmitt, R. G. Moore, S. Johnston, Y.-T. Cui, W. Li, M. Yi, Z. K. Liu, M. Hashimoto, Y. Zhang, D. H. Lu, T. P. Devereaux, D.-H. Lee, and Z.-X. Shen, Interfacial mode coupling as the origin of the enhancement of T_C in FeSe films on $SrTiO_3$, Nature (London) **515**, 245 (2014).

[21] D.-H. Lee, What makes the T_c of $FeSe/SrTiO_3$ so high? Chin. Phys. B **24**, 117405 (2015).

[22] Z.-X. Li, F. Wang, H. Yao, and D.-H. Lee, What makes the T_c of monolayer FeSe on $SrTiO_3$ so high: a sign-problem-free quantum Monte Carlo study, Sci. Bull. **61**, 925 (2016).

[23] L. Rademaker, Y. Wang, T. Berlijn, and S. Johnston, Enhanced superconductivity due to forward scattering in FeSe thin films on $SrTiO_3$ substrates, New J. Phys. **18**, 022001 (2016).

[24] S. Choi, S. Johnston, W.-J. Jang, K. Koepernik, K. Nakatsukasa, J. M. Ok, H.-J. Lee, H. W. Choi, A. T. Lee, A. Akbari, Y. K. Semertzidis, Y. Bang, J. S. Kim, and J. Lee, Enhancement of Superconductivity by Interfacial Phonons in Perovskite-Clad FeAs Monolayers, Phys. Rev. Lett. **119**, 107003 (2017).

[25] Q. Song, T. L. Yu, X. Lou, B. P. Xie, H. C. Xu, C. H. P. Wen, Q. Yao, S. Y. Zhang, X. T. Zhu, J. D. Guo, R. Peng, and D. L. Feng, Phonon-enhanced superconductivity at the $FeSe/SrTiO_3$ interface, arXiv:1710.07057.

[26] J. Jandke, F. Yang, P. Hlobil, T. Engelhardt, K. Zakeri, C. Gao, J. Schmalian, and W. Wulfhekel, Unconventional pairing in single FeSe layers, arXiv:1710.08861.

[27] F. Li and G. A. Sawatzky, Electron-phonon coupling versus photoelectron energy loss at the origin of replica bands in photoemission of FeSe on $SrTiO_3$, arXiv:1710.10795.

[28] M. Rahlenback, G. L. Sun, C. T. Lin, B. Keimer, and C. Ulrich, Phonon anomalies in pure and underdoped $R_{1-x}K_xFe_2As_2$ (R = Ba,Sr) investigated by Raman light scattering, Phys. Rev. B **80**, 064509 (2009).

[29] B. Xu, Y. M. Dai, B. Shen, H. Xiao, Z. R. Ye, A. Forget, D. Colson, D. L. Feng, H. H. Wen, C. C. Homes, X. G. Qiu, and R. P. S. M. Lobo, Anomalous phonons redshift in K-doped $BaFe_2As_2$ iron pnictides, Phys. Rev. B **91**, 104510 (2015).

[30] T. Dong, Z. G. Chen, R. H. Yuan, B. F. Hu, B. Cheng, and N. L. Wang, Formation of partial energy gap below the structural phase transition and the rare-earth element-substitution effect on infrared phonons in ReFeAsO (Re = La,Nd, and Sm), Phys. Rev. B **82**, 054522 (2010).

[31] S. Gerber, S.-L. Yang, D. Zhu, H. Soifer, J. A. Sobota, S. Rebec, J. J. Lee, T. Jia, B. Moritz, C. Jia, and A. Gauthier, Y. Li, D. Leuenberger, Y. Zhang, L. Chaix, W. Li, H. Jang, J.-S. Lee, M. Yi, G. L. Dakovski, S. Song, J. M. Glownia, S. Nelson, K. W. Kim, Y.-D. Chuang, Z. Hussain, R. G. Moore, T. P. Devereaux, W.-S. Lee, P. S. Kirchmann, and Z.-X. Shen, Femtosecond electron-phonon lock-in by photoemission and x-ray free-electron laser, Science **357**, 71 (2017).

[32] L. Boeri, O. V. Dolgov, and A. A. Golubov, Is $LaFeAsO_{1-x}F_x$ an Electron-Phonon Superconductor? Phys. Rev. Lett. **101**, 026403 (2008).

[33] T. Saito, S. Onari, and H. Kontani, Orbital fluctuation theory in iron pnictides: Effects of As-Fe-As bond angle, isotope substitution, and Z^2-orbital pocket on superconductivity, Phys. Rev. B **82**, 144510 (2010).

[34] F. Yndurain and J. M. Soler, Anomalous electron-phonon interaction in doped LaFeAsO: First-principle calculations, Phys. Rev. B **79**, 134506 (2009).

[35] S. Li, E. Khatami, and S. Johnston, Competing phases and orbital-selective behaviors in the two-orbital Hubbard-Holstein model, Phys. Rev. B **95**, 121112(R) (2017).

[36] S. Coh, M. L. Cohen, and S. G. Louie, Antiferromagnetism enables electron-phonon coupling in iron-based superconductors, Phys. Rev. B **94**, 104505 (2016).

[37] N. Dupuis, C. Bourbonnais, and J. C. Nickel, Superconductivity and antiferromagnetism in quasi-one-dimensional organic conductors, Low Temp. Phys. **32**, 380 (2006).

[38] E. A. Nowadnick, S. Johnston, B. Moritz, R. T. Scalettar, and T. P. Devereaux, Competition Between Antiferromagnetic and Charge-Density-Wave Order in the Half-Filled Hubbard-Holstein Model, Phys. Rev. Lett. **109**, 246404 (2012).

[39] J. Bauer and A. C. Hewson, Competition between antiferromagnetic and charge order in the Hubbard-Holstein model, Phys. Rev. B **81**, 235113 (2010).

[40] Y. Murakami, P. Werner, N. Tsuji, and H. Aoki, Ordered phases in the Holstein-Hubbard model: Interplay of strong Coulomb interaction and electron-phonon coupling, Phys. Rev. B **88**, 125126 (2013)

[41] S. Pradhan and G. Venketeswara Pai, Holstein-Hubbard model at half filling: A static auxiliary field study, Phys. Rev. B **92**, 165124 (2015).

[42] R. T. Clay and R. P. Hardikar, Intermediate Phase of the One Dimensional Half-Filled Hubbard-Holstein Model, Phys. Rev. Lett. **95**, 096401 (2005).

[43] R. P. Hardikar and R. T. Clay, Phase diagram of the one-dimensional Hubbard-Holstein model at half and quarter filling, Phys. Rev. B **75**, 245103 (2007).

[44] W. Koller, D. Meyer, and A. C. Hewson, Dynamic response of functions for the Holstein-Hubbard model, Phys. Rev. B **70**, 155103 (2004).

[45] C. B. Mendl, E. A. Nowadnick, E. W. Huang, S. Johnston, B. Moritz, and T. P. Devereaux, Doping dependence of ordered phases and emergent quasiparticles in the doped Hubbard-Holstein model, Phys. Rev. B **96**, 205141 (2017).

[46] G. S. Jeon, T.-H. Park, J. H. Han, H. C. Lee, and H.-Yong Choi, Dynamical mean-field theory of the Hubbard-Holstein model at half filling: Zero temperature metal-insulator and insulator-insulator transitions, Phys. Rev. B **70**, 125114 (2004).

[47] S. Johnston, E. A. Nowadnick, Y. F. Kung, B. Moritz, R. T. Scalettar, and T. P. Devereaux, Determinant quantum Monte Carlo study of the two-dimensional single-band Hubbard-Holstein model, Phys. Rev. B **87**, 235133 (2013).

[48] E. H. Lieb and F. Y. Wu, Absence of Mott Transition in an Exact Solution of the Short-Range, One-Band Model in One Dimension, Phys. Rev. Lett. **20**, 1445 (1968).

[49] J. E. Hirsch and E. Fradkin, Effect of Quantum Fluctuations on the Peierls Instability: A Monte Carlo Study, Phys. Rev. Lett. **49**, 402 (1982).

[50] J. E. Hirsch and E. Fradkin, Phase diagram of one-dimensional electron-phonon systems. II. The molecular-crystal model, Phys. Rev. B **27**, 4302 (1983).

[51] R. J. Bursill, R. H. Mckenzie, and C. J. Hamer, Phase Diagram of the One-Dimensional Holstein Model of Spinless Fermions, Phys. Rev. Lett. **80**, 5607 (1998).

[52] E. Jeckelmann, C. Zhang, and S. R. White, Metal-insulator transition in the one-dimensional Holstein model at half filling, Phys. Rev. B **60**, 7950 (1999).

[53] E. Fradkin and J. E. Hirsch, Phase diagram of one-dimensional electron-phonon systems. I. The Sy-Schrieffer-Heeger model, Phys. Rev. B **27**, 1680 (1983).

[54] M. Capone, G. Sangiovanni, C. Castellani, C. Di Castro, and M. Grilli, Phase Separation Close to the Density-Driven Mott Transition in The Hubbard-Holstein Model, Phys. Rev. Lett. **92**, 106401 (2004).

[55] S. Kumar and J. van den Brink, Charge ordering and magnetism in quarter-filled Hubbard-Holstein model, Phys. Rev. B **78**, 155123 (2008).

[56] S. Reja, S. Yarlagadda, and P. B. Littlewood, Phase diagram of the one-dimensional Hubbard-Holstein model at quarter filling, Phys. Rev. B **84**, 085127 (2011).

[57] H. Kontani and S. Onari, Orbital-Fluctuation-Mediated Superconductivity in Iron Pnictides: Analysis of the Five-Orbital Hubbard-Holstein Model, Phys. Rev. Lett. **104**, 157001 (2010).

[58] T. Yamada, J. Ishizuka, and Y. Ōno, Metal-insulator transition and superconductivity in the two-orbital Hubbard-Holstein model for iron-based superconductors, J. Phys. Soc. Jpn. **83**, 044711 (2014)

[59] M. Capone, M. Fabrizio, C. Castellani, and E. Tosatti, Strongly correlated superconductivity, Science **296**, 2364 (2002).

[60] M. Capone, M. Fabrizio, and E. Tosatti, Direct Transition Between a Singlet Mott Insulator and a Superconductor, Phys. Rev. Lett. **86**, 5361 (2001).

[61] J. E. Han, O. Gunnarsson, and V. H. Crespi, Strong Superconductivity with Local Jahn-Teller Phonons in C_{60} Solids, Phys. Rev. Lett. **90**, 167006 (2003).

[62] E. Y. Loh, Jr., J. E. Gubernatis, R. T. Scalettar, S. R. White, D. J. Scalapino, and R. L. Sugar, Sign problem in the numerical simulation of many-electron systems, Phys. Rev. B **41**, 9301 (1990).

[63] C. Castellani, C. Di Castro, D. Feinberg, and J. Ranninger, New Model Hamiltonian for the Metal-Insulator Transition, Phys. Rev. Lett. **43**, 1957 (1979).

[64] M. Daghofer, A. Nicholson, A. Moreo, and E. Dagotto, Three orbital model for the iron-based superconductors, Phys. Rev. B **81**, 014511 (2010).

[65] R. Blankenbecler, D. J. Scalapino, and R. L. Sugar, Monte Carlo calculations of coupled boson-fermion systems. I, Phys. Rev. D **24**, 2278 (1981).

[66] S. R. White, D. J. Scalapino, R. L. Sugar, E. Y. Loh, J. E. Gubernatis, and R. T. Scalettar, Numerical study of the two-dimensional Hubbard model, Phys. Rev. B **40**, 506 (1989).

[67] C.-C. Chang, S. Gogolenko, J. Perez, Z. Bai, and R. T. Salettar, Recent advances in determinant quantum Monte Carlo, Philos. Mag. B **95**, 1260 (2013).

[68] R. T. Scalettar, N. E. Bickers, and D. J. Scalapino, Competition of pairing and Peierls-charge-density-wave correlations in a two-dimensional electron-phonon model, Phys. Rev. B **40**, 197 (1989).

[69] M. Jarrell and J. E. Gubernatis, Bayesian interference and the analytic continuation of imaginary-time quantum Monte Carlo data, Phys. Rep. **269**, 133 (1996).

[70] S. Fuchs, T. Pruschke, and M. Jarrell, Analytic continuation of quantum Monte Carlo data by stochastic analytical inference, Phys. Rev. E **81**, 056701 (2010).

[71] P. Maurel and M.-B. Lepetit, Optical phonons in a quarter-filled one-dimensional Hubbard model, Phys. Rev. B **62**, 10744 (2000).

[72] N. Trivedi and M. Randeria, Deviations from Fermi-Liquid Behavior Above T_c in 2D Short Coherence Length Superconductors, Phys. Rev. Lett. **75**, 312 (1995).

[73] E. A. Nowadnick, S. Johnston, B. Moritz, and T. P. Devereaux, Renormalization of spectra by phase competition in the half-filled Hubbard-Holstein model, Phys. Rev. B **91**, 165127 (2015).

[74] M. Hohenadler, D. Neuber, W. von der Linden, G. Wellein, J. Loos, and H. Fehske, Photoemission spectra of many-polaron systems, Phys. Rev. B **71**, 245111 (2005).